Available online at www.sciencedirect.com

ScienceDirect

International Journal of Heat and Mass Transfer 50 (2007) 919–930

International Journal of HEAT and MASS TRANSFER

www.elsevier.com/locate/ijhmt

Endwall heat transfer and fluid flow around an inclined short cylinder

I.K. Choi [a], T. Kim [b,*], S.J. Song [a], T.J. Lu [b]

[a] *School of Mechanical and Aerospace Engineering, Seoul National University, Seoul 151-744, Republic of Korea*
[b] *School of Aerospace, Xi'an Jiaotong University, Xi'an 710049, PR China*

Received 4 January 2006; received in revised form 8 August 2006
Available online 17 October 2006

Abstract

Measurements of endwall heat transfer and flow field around a short single cylinder have been performed to examine the influence of cylinder inclination at low Reynolds number ($Re_D = 1.0 \times 10^4$). Both ends of the cylinder are attached to the endwalls and the length-to-diameter ratio of the cylinder varies from 2.7 to 4, depending on the inclination angle. Endwall heat transfer contours (obtained from transient liquid crystals) and endwall flow visualization results consistently indicate that the interaction between the horseshoe vortices around the cylinder and the wakes shed from the cylinder varies with the inclination. Spanwise pressure gradient induced by the inclination causes: (i) skewing of the upstream main flow as it approaches the cylinder; (ii) formation of a jet-like flow immediately downstream of the cylinder, followed by its impingement onto the endwall; and (iii) skewed separation line along the cylinder span from the cylinder axis.

Keywords: Endwall surface heat transfer; Horseshoe vortex; Inclined single cylinder; Spanwise pressure gradient; Wakes

1. Introduction

The crossflow around cylinders having various cross sections (e.g., triangle, square, and circle) has been well documented [1–7]. In engineering applications, such cylinders can be isolated or grouped into bundles. The simplest cross-sectional geometry is perhaps the circle. The flow around an infinitely long cylinder with a circular cross section can be treated as two-dimensional, i.e. the velocity component parallel to the cylinder axis plays no part in the flow; see Zdravkovich [3,4], Sparrow and Yanez Moreno [6]. The flow external to the circular bar approaches the cylinder in crossflow (relative to the cylinder axis).

For cylinders with a finite length (or span), the geometrical conditions of the cylinder ends (e.g. open ends and endwall attached ends) are critical for flow properties near the ends. If one of the cylinder ends is open to the mainstream flow while the other is attached to the endwall plate, the distinct flow features are the shear layers developed from the open end (tip) which change the wake patterns behind the cylinder near the tip region. This may be analogous to the flow past, for example, chimneys and circular buildings. According to Sumner et al. [8], the tip vortex structure is distinct and not a representation of the "Kármán vortices." In such cases, the length-to-diameter ratio plays an important role in determining flow structures behind the cylinder and near the endwall (or ground). At the endwall, a classical vortical structure, the so-called "horseshoe vortex", is formed around a vertex. In accordance with Kelvin's circulation theorem, the boundary layer vorticity cannot be destroyed. Instead, it is convected around each side of the cylinder to form the two legs of the horseshoe vortex.

In some engineering applications, a single cylinder with both ends attached to endwalls is positioned at a certain angle of attack (inclination) to the mainstream flow (or the flow approaches the cylinder at an inclined angle). Fig. 1 shows high aspect ratio rotor blades which are

---

[*] Corresponding author. Tel.: +86 138 9194 1189.
E-mail address: tongbeum@gmail.com (T. Kim).

0017-9310/$ - see front matter © 2006 Elsevier Ltd. All rights reserved.
doi:10.1016/j.ijheatmasstransfer.2006.08.012

Nomenclature

D	cylinder diameter (m)
h	convection heat transfer coefficient (W/m^2 K)
H, W, L	height, width and length of test section (m)
l	cylinder length (span) (m)
N	nodal point
Nu_D	Nusselt number based on cylinder diameter
Re_D	Reynolds number based on cylinder diameter
S	saddle point
U	mainstream velocity at inlet of test section (m/s)
X, Y, Z	coordinate system
z'	coordinate along the cylinder axis
α	inclination angle (°)
ρ	density of air (kg/m^3)

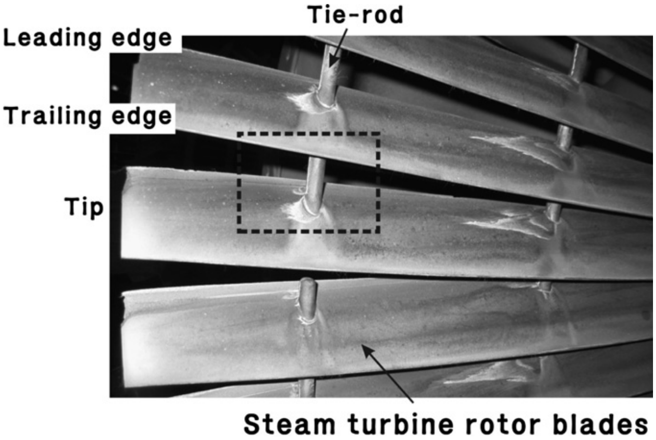

Fig. 1. A photograph of steam turbine rotors showing rotor blades connected by a circular tie-rod (from Seochun Power Plant, Korea Midland Power Co., South Korea).

connected by circular tie-rods to reduce vibration during operation. Notice that horseshoe vortices are formed at each vertex. Furthermore, heat transfer takes place from the hot fluid flow (heated during compression) to the cold endwalls (rotor blades in this case) and the cylinder itself. In this case, the local heat transfer distribution around the cylinder depends on the above mentioned flow structures.

Local heat transfer around an upright circular cylinder confined between endwall plates has been previously investigated [1–5]. However, heat transfer and flow around an inclined cylinder confined between endwalls has not yet been reported. The present study focuses on this problem and examines how the inclination of the cylinder affects the local endwall surface heat transfer. Comprehensive measurements including detailed endwall surface flow/heat transfer, cylinder surface flow, and flow fields behind the cylinder are carried out for five different inclination angles using both water- and wind-tunnels.

2. Experimental details

2.1. Wind- and water-tunnel facilities

Two different sets of experiments have been conducted using wind- and water-tunnels. Firstly, an open-type wind-tunnel was used for flow visualization and heat transfer experiments, including cylinder/endwall surface flow visualization and endwall heat transfer mapping using thermochromic liquid crystal (TLC). A centrifugal fan blows air that passes through a settling chamber, screens, and a contraction section. A schematic of the test section is illustrated in Fig. 2, which shows the TLC coated test channel wall and an image acquisition setup. Details associated with the TLC measurements and data reduction procedure are discussed in Section 2.3.

Secondly, a closed-type water-tunnel has been built to visualize the flow around the cylinder and near the endwalls (not shown in this paper). As a set of discs spins, water is drawn due to the friction between the disc surfaces and water. Water passes through guide vanes and a contraction section. Honeycombs and a screen are used for flow conditioning.

2.2. Cylinder configurations

Single circular cylinders with inclination angles of $\alpha = 0°$, 15°, 30°, 40° and 45° have been tested. The inclination angle α is measured from the z-axis, which is normal to the mainstream flow direction. Positive inclination angle indicates counter-clockwise rotation with respect to the y-axis (along the channel width). Thus, the cylinder is rotated clockwise as its inclination angle increases.

Typically, two different methods can be used to change the inclination of a cylinder. One is to fix both ends of the cylinder to the endwall plates. When the lower endwall plate is shifted longitudinally and upward, the angle between the mainstream and the cylinder axis increases. During this inclination, the cylinder length remains unchanged. Another way, which is employed in the present study, is to fix the channel height (H) and rotate the cylinder with respect to the y-axis. The consequence is that the length (l) of the cylinder sandwiched between the channel endwalls is increased according to $l = H/\cos(\alpha)$. The parameters of the cylinder models and the test channel are listed in Table 1.

2.3. Surface heat transfer mapping using thermochromic liquid crystal

For thermal mapping of the endwall surfaces, transient thermochromic liquid crystal (TLC) technique has been

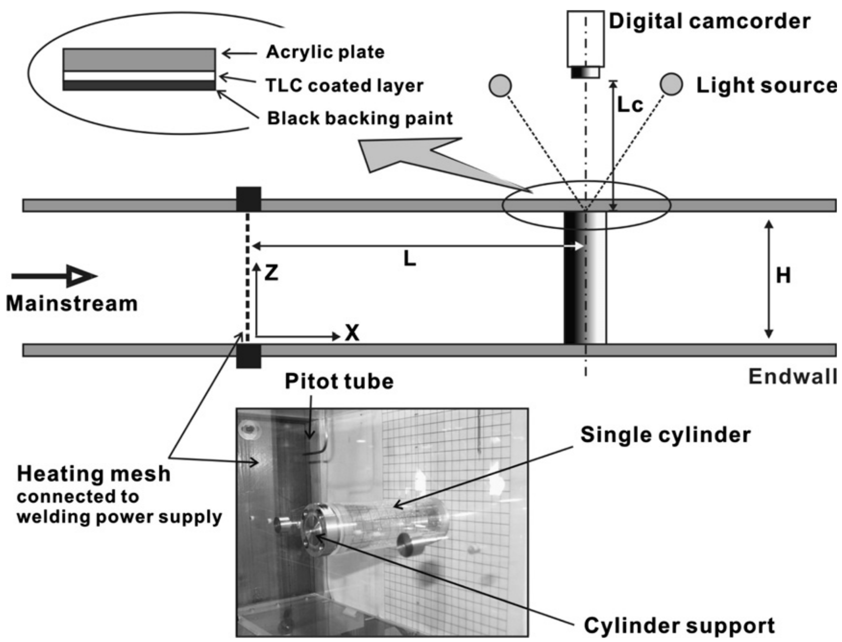

Fig. 2. Schematic of test rig and a photograph showing test section used in the wind-tunnel for flow measurements, endwall heat transfer, and visualization.

Table 1
Parameters of single cylinder test models for flow measurements in wind-tunnel and flow visualization in water-tunnel

Inclination angle α (°)	Cylinder			Channel		Blockage ratio D/W
	Diameter D (mm)	Length l (mm)	l/D	Width W (mm)	Height H (mm)	
0	30	80.0	2.67	200	80	0.15
15		82.8	2.76			
30		92.4	3.08			
40		104.4	3.48			
45		113.1	3.77			

employed. A sudden increase in the fluid temperature has been obtained by a heating mesh that consists of fine wire meshes (36 μm diameter with 38% open area ratio) and brass bus bars. Adjustment of the electric current from a welding power supply enables the control of heat input to fluid flow.

During the transient heat transfer experiments, the air temperature increases exponentially with time, described in non-dimensional form by

$$\Theta_{\mathrm{f}}(t) = \frac{T_{\mathrm{f}}(t) - T_{\mathrm{init}}}{T_{\mathrm{ref}} - T_{\mathrm{init}}} = 1 - \mathrm{e}^{-t/\tau_2} \tag{1}$$

where $T_{\mathrm{f}}(t)$ is the inlet fluid temperature measured downstream of the heating mesh; T_{init} is the initial fluid temperature; T_{ref} is a reference temperature (to be defined later); and τ_2 is the representative time constant, or the time required for the dimensionless temperature to reach 0.632 ($\sim$3.0 s for $Re_{\mathrm{D}} = 1.0 \times 10^4$). Details associated with the heating mesh can also be found in [9].

When the flow temperature is suddenly raised to the reference temperature T_{ref}, evaluation of the adiabatic wall temperature T_{adw} is necessary [10] because the actual temperature of the flow may differ due to the effect of frictional heating. The adiabatic wall temperature is defined as

$$T_{\mathrm{adw}} = T_{\mathrm{ref}} + RU^2/2c_p \tag{2}$$

where R is a recovery factor, U is the mainstream velocity, c_p is the specific thermal capacity of the fluid, and T_{ref} is the static temperature of the mainstream. Typical operating conditions in this study are: R ($=Pr^{1/2}$) ~ 0.843 for air, $U \sim 5.0$ m/s and $c_p = 1003$ J/kg K. The adiabatic temperature then becomes $T_{\mathrm{adw}} \approx T_{\mathrm{ref}}$ due to the low velocity of fluid flow and is typically assumed to be invariant in time [11]. In the following sections, the adiabatic wall temperature will be used as the reference temperature.

The non-dimensional temperature variation at the boundary surface when the flow temperature exhibits exponential rise is derived from Gillespie [12]:

$$\Theta_{\mathrm{S}}(t,\tau) = \frac{T_{\mathrm{S}}(t) - T_{\mathrm{init}}}{T_{\mathrm{adw}} - T_{\mathrm{init}}} = f(\beta, \beta_\tau) \tag{3}$$

where $T_{\mathrm{S}}(t) - T_{\mathrm{init}} = f(\beta, \beta_{\tau_2})[T_{\mathrm{adw}} - T_{\mathrm{init}}]$;

$$f(\beta,\beta_\tau) = 1 - \frac{1}{1+\beta_\tau^2}\mathrm{e}^{\beta^2}\mathrm{erfc}(\beta) - \mathrm{e}^{-t/\tau}\frac{\beta_\tau^2}{1+\beta_\tau^2} \times \left\{1 + \frac{1}{\beta_\tau}\left[\frac{1}{\pi}\sqrt{\frac{t}{\tau}} + \frac{2}{\pi}\sum_{n=1}^{\infty}\frac{1}{n}\mathrm{e}^{-n^2/4}\sinh\left(n\sqrt{\frac{t}{\tau}}\right)\right]\right\}$$

$\beta = h\sqrt{\alpha t}/k$; $\beta_\tau = h\sqrt{\alpha\tau}/k$; h is the convection heat transfer coefficient to be obtained, α is the thermal diffusivity of the acryl plate; and τ is the time constant that depends on the performance of the heating mesh. For a prescribed value of the convection heat transfer coefficient h, Eq. (3) produces a temporal variation of the temperature difference $T(t) - T_{\text{init}}$.

2.4. Flow visualization techniques

Both cylinder and endwall surface flow patterns have been visualized using an oil–dye mixture technique in the wind-tunnel. Florescent powder is mixed with a light diesel fuel, and the mixture is then applied to the cylinder surface. When the aerodynamic shear stresses redistribute the mixture, visualization of the surface flow patterns is realized. Before the application of the mixture, the surface is painted in black. This painting is done to enhance the reflectivity when using ultraviolet light to illuminate the surface flow pattern while it is being photographed. To observe flow around a cylinder of diameter D in the water-tunnel, an ink–dye solution with a specific gravity similar to water is injected through a small steel tube (0.5 mm inner diameter). The tube exit where the ink–dye particles are released, is located at $5D$ distance upstream from the cylinder. The streaklines are then captured through transparent endwalls and sidewalls by a SONY™ digital camcorder.

2.5. Velocity and flow angle measurements

The time-averaged flow quantities, including flow angles and stagnation pressures, have been measured at selected downstream traverse planes ($x/D = 2$ and 4) using a five-hole probe (head diameter = 3 mm, United Sensor™) and a Kiel probe, respectively. A stagnation pressure port of the five-hole probe is aligned with the nominal flow direction, x-axis for the selected y–z traverse planes. The probe is mounted on an automated two-dimensional traverse system so that velocity vectors could be obtained in each traverse plane. Pressure tubes of the probes are connected to a 48 port J-type Scanivalve™. In addition, a Pitot tube is positioned at $2.5D$ upstream from the cylinder to monitor the mainstream velocity.

3. Variation of endwall thermal and surface flows

3.1. Endwall heat transfer

3.1.1. Overall observation

This section presents the variation of endwall surface heat transfer with inclination angle. For heat transfer between endwall surfaces and mainstream flow, the cylinder acts to increase convection heat transfer like a turbulator or a protruded fin. Vortical structures such as the "horseshoe vortex" form around the cylinder. Fig. 3(a) shows the map of endwall convection heat transfer coefficient h for a cylinder with 'zero' inclination angle. A high heat transfer region in front of the cylinder's leading edge results from the stagnation of flow. The white background area designated the "undefined region" is caused by the non-detectable response of the TLC to low temperature change in time and magnitude in this region. Therefore, the convection heat transfer coefficient h could not be determined. Another white region near/on the cylinder indicates a separation bubble where a low momentum fluid is trapped, leading to the lack of TLC response to the temperature change.

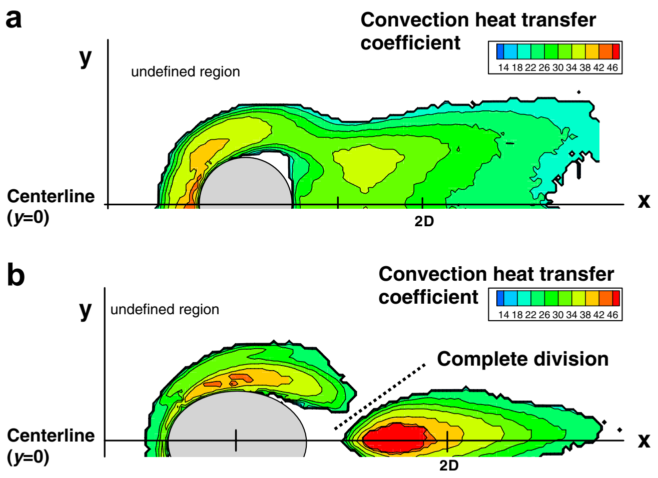

Fig. 3. Contours of endwall surface convection heat transfer coefficients (h) on the lower endwall at $Re_{\mathrm{D}} = 1.0 \times 10^4$: (a) 0°; (b) 45°.

A relatively high heat transfer region (but not comparable to that of the stagnation region) behind the cylinder is observed at about $1.5D$ downstream from the cylinder axis and $0.5D$ away from the centerline. This region results from the interaction of the horseshoe vortex tails with the endwall surface.

The uncertainty, with a 95% confidence interval, associated with the heat transfer coefficient measurement is estimated to be less than 6.3%. The uncertainty has been estimated using the method of Coleman and Steele [13]. More details of the TLC technique can be found in [9–11,14]. Prior to the heat transfer analysis, buoyancy effect is estimated to be negligible due to low operating temperature range i.e. less than 20 K in this study. A ratio of Gr_{D} to Re_{D}^2 is about 0.001 where Gr_{D} is the Grashof number defined as $Gr_{\mathrm{D}} = g\beta\Delta \mathrm{T}\mathrm{V}/\nu^2$ [15]. Here, g is the gravity, β is the coefficient of thermal expansion, ΔT is the temperature difference, V is the representative volume (=cylinder diameter^3), and ν is the kinematic viscosity of air. In addition, since a low thermal conductivity material (Perspex, $k_s \sim 0.2$ W/mK) has been used for the cylinder, it is reasonable to assume that conduction through the cylinder is negligible in this study.

Fig. 3(b) displays the endwall heat transfer coefficient contour of the 45° inclined cylinder. The stagnation region of high heat transfer becomes thinner with increasing α. This may be associated with the change of vortical structures around the cylinder vertex including the "horseshoe vortex" as a result of the cross-sectional shape change (from circular to elliptical). Analysis of this variation is discussed in Section 3.2.

The most distinctive feature occurs at the aft cylinder. As inclining the cylinder, a peak value of the heat transfer coefficient behind the cylinder e.g. at 1.75*D* on top of the centerline ($y = 0$) becomes comparable to that at the upstream stagnation region for $\alpha = 30°$ (figure is not shown). A further inclination of the cylinder to $\alpha = 45°$ intensifies the magnitude of the heat transfer rate in that region which moves upstream to 1.5*D* (Fig. 3(b)). Moreover, the downstream high heat transfer region divides into two regions – one under the influence of the horseshoe vortex and the other affected by the flow behind the cylinder. At the boundary between the two regions on the endwall surface, shear stress is so low that the TLC particles do not respond to the negligible temporal change of temperature there.

3.1.2. Centerline Nusselt number variation with inclination

To elaborate on the effect of inclination on the endwall surface heat transfer, the data from the center line ($y = 0$) of the cylinder are plotted in Fig. 4 as a function of the axial distance (x/D). Here, the Nusselt number is based on the cylinder diameter and is defined as

$$Nu_{\mathrm{D}} = \frac{hD}{k_{\mathrm{f}}}$$

where h is the convection heat transfer coefficient obtained from the TLC measurements and k_{f} is the thermal conductivity of air. Since the cross-sectional shape of the cylinder on the endwall changes with the inclination of the cylinder along the flow direction, the cylinder diameter in the x-axis varies as a function of the inclination angle as $D(\alpha) = D/\cos(\alpha)$ while that in the y-axis remains unchanged. Therefore, the endwall surface Nusselt numbers could only be obtained for $x/D \leqslant -(x/D)/(2\cos(\alpha))$ in the fore cylinder region and $+(x/D)/(2\cos(\alpha)) \leqslant x/D$ in the aft cylinder region along the centerline ($y = 0$). For example $(x/D)/(2\cos(\alpha))$ is approximately 0.577 for $\alpha = 30°$ and 0.707 for $\alpha = 45°$.

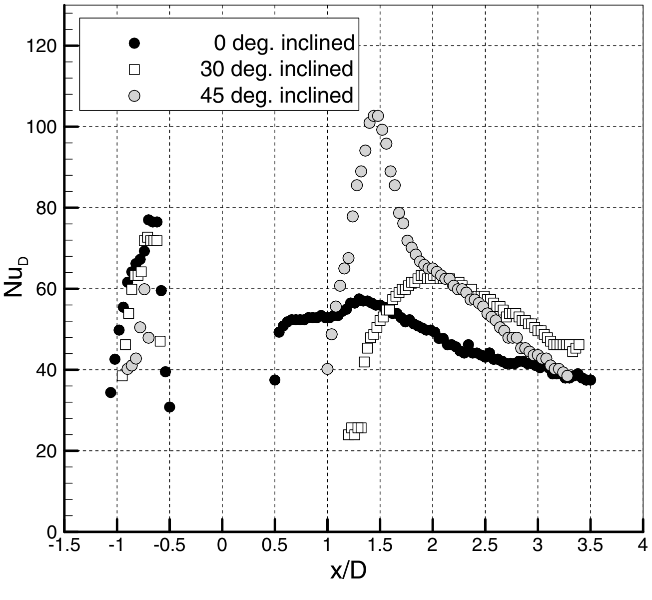

Fig. 4. A comparison of streamwise Nusselt number distribution along the centerline ($y = 0$) of the cylinder (lower endwall).

For all of the cases considered, along the centerline, the Nusselt numbers increase as the upstream flow approaches the leading edge. This is caused by the flow stagnation and formation of the "horseshoe vortex" immediately upstream of the cylinder's leading edge. Subsequently, a sudden drop in the heat transfer follows due to the presence of a pair of counter-rotating vortices between the horseshoe vortex and the front surface of the cylinder, Praisner et al. [16]. Increasing α reduces the magnitude of the Nusselt numbers, but the overall trend remains unchanged. Focusing on the aft cylinder for the upright cylinder, the Nusselt number gradually rises, peaks at approximately 1.25*D*, and then begins to decrease. For $\alpha = 30°$, a relatively wide gap, which indicates very little heat transfer, is present between the aft cylinder and the 1.25*D* downstream location. Downstream of this region, the Nusselt number increases steeply along the x-axis, peaking at about 2.0*D*. With further inclination up to 45°, the gap is narrowed. The Nusselt number reaches its peak value at 1.5*D* which is larger than that measured at the leading edge of the cylinder. The inclination leads to the relocation of the peak heat transfer location towards the trailing edge of the cylinder. The reasoning behind this relocation will be examined using flow measurements in the following sections.

3.2. Topology of endwall surface flows

3.2.1. Lower endwall

The kinematics of surface flow around a single cylinder placed normal to the endwall surface has been well established. Therefore, only a brief description of the topological classification of the endwall surface flow is addressed here, following the definitions of Hunt et al. [17]. Since only the time averaged behavior of the surface flow has been marked, the endwall flow pattern (horseshoe vortex) in the z–x plane is symmetric with respect to the cylinder axis. Conventionally, the saddle point (S) refers to a point through which two particular streamlines pass. Each line acts as a barrier in the field of limiting streamlines so that one set of streamlines cannot cross another set of streamlines. One of the saddle points is located at about 1.5*D* upstream from the cylinder axis (or 1*D* from the leading edge), denoted as S_1 (Fig. 5(a)). Another saddle point is found in the vicinity of the cylinder leading edge, S_2. The formation of the saddle point results from the interaction of two counter-rotating vortices; see Praisner et al. [16]. The horseshoe vortex legs merge at approximately 2*D* downstream, forming saddle point S_3 there. In addition, a nodal point N, which is a singular point common to an infinite number of limiting streamlines, is observed behind the cylinder. The nodal point is indicated by the black background because all of the painted oil–dye particles have been lifted off due to the vortical action at the node.

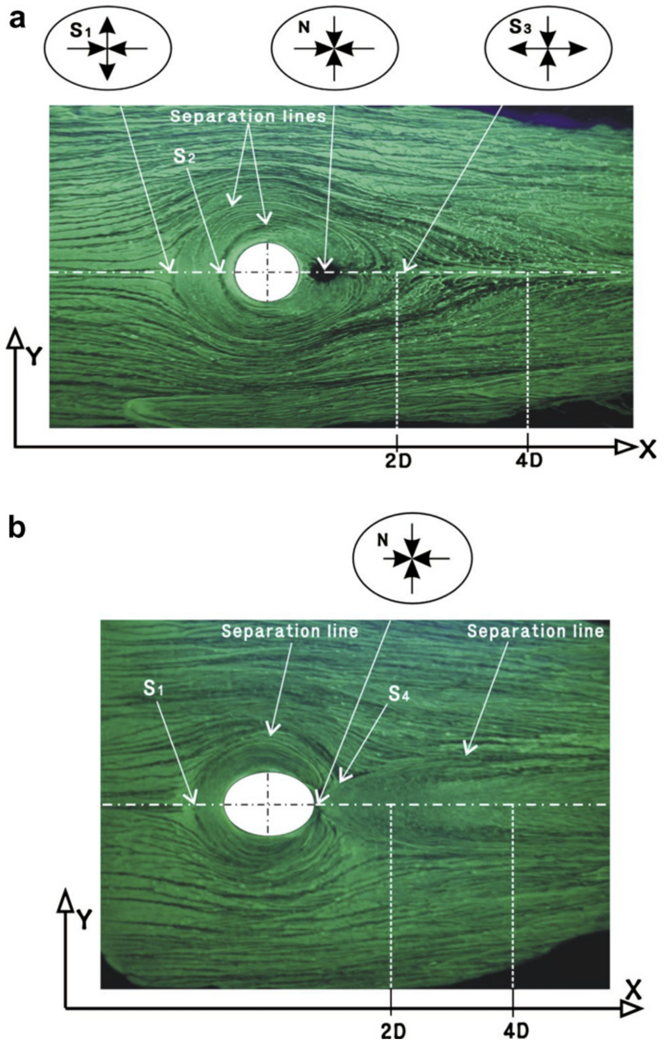

Fig. 5. Visualized surface flow images on the lower endwall with four different inclined angles at $Re_D = 1.0 \times 10^4$: (a) 0°; (b) 45°.

Mainstream turbulence and inlet boundary layer thickness have been measured to be 0.9% and $0.1H$, respectively, at $1D$ upstream from the leading edge of the cylinder. Here H is the channel height and D is the cylinder diameter.

With inclination, distinct changes are visible in the behavior of the horseshoe vortex, as shown in Fig. 5(b). Due to the backward cylinder inclination on the lower endwall, there is a velocity component induced along the stagnation line of the cylinder parallel to the cylinder axis; the stagnated flow is "released". Consequently, the horseshoe vortex core is moved closer to the stagnation point on the endwall. This causes the thinning of the stagnation heat transfer region as observed in Figs. 3 and 4. Furthermore, there appears a region where both legs of the horseshoe vortex are separated with inclination, whereas they are merged along the centerline in the upright cylinder. Separation lines that act as boundaries between the two legs of the horseshoe vortex and an "inclination induced region" become clear with increasing inclination angle (results from 15°, 30° and 40° are not shown here due to the limited length of the paper but can be found in [18]). Both legs of the horseshoe vortex interact with the flow separated from the inclined cylinder surface, forming saddle point S_4 at the separation lines. It can be concluded that the high heat transfer region behind the cylinder is associated with the reattachment of the inclined wakes shed from the cylinder surface. Furthermore, the division of the endwall heat transfer region into two regions aft of the cylinder results from the formation of the separation lines which intersect the tails of the horseshoe vortex.

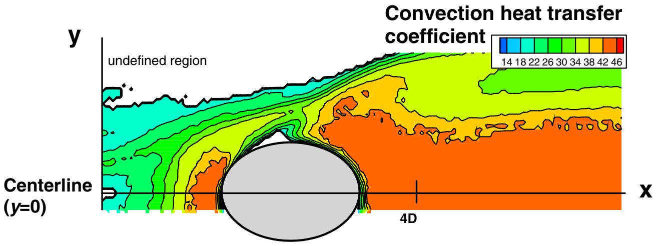

Fig. 6. Contour of endwall surface convection heat transfer coefficient (h) on the upper endwall with 45° inclined angle at $Re_D = 1.0 \times 10^4$.

3.2.2. Upper endwall

The inclination causes asymmetry of the mainstream flow with respect to the midspan of the cylinder (x–y plane). This implies that the vertices at the lower and upper endwalls create different flow patterns. For a given inclination angle, e.g. $\alpha = 45°$, the mainstream flow experiences different geometries of the vertex, leading to different endwall surface heat transfer patterns. Fig. 6 shows the contour of endwall heat transfer coefficients on the upper endwall. Compared to that of the lower endwall (Fig. 3(b)), the separation bubble, indicated by a white region near the ellipse surface, has moved closer to the leading edge. In comparison with the lower endwall, a smaller high heat transfer region is seen in the stagnation region whereas a much wider high heat transfer region is observed at the aft cylinder. The cause of the observed heat transfer pattern around the upper vertex is the existence of an additional spanwise velocity component directed towards the upper endwall. To support this argument, the flow field information around the entire cylinder away from the endwalls is provided in the following section.

4. Flow around a circular cylinder

The endwall surface heat transfer is determined by the endwall surface flow characteristics, which are also consequences of the interaction amongst the mainstream flow, cylinders, and the endwalls. To further address the issue of how the inclined configuration influences the mainstream flow, the flow fields around the cylinder are discussed in this section.

4.1. Flows around the single cylinder

It is common to witness the formation of a Kármán eddy street when a fluid flows past a stationary cylinder placed normal to mainstream flow. The cylinder considered here has a short aspect ratio (=l/D) of 2.7 and is sandwiched between the endwalls. The wake pattern is characterized by a dimensionless wake shedding frequency, i.e. the Strouhal number ($S_t = f/U$), where f is the shedding frequency measured at the $2D$ downstream from the one side edge of the cylinder. In the present study, S_t was found to be 0.195 at $Re_D = 1.0 \times 10^4$ for the non-inclined cylinder, showing good agreement with the data reported in open literature [3,4].

Fig. 7 shows flow visualization results obtained from the water-tunnel experiments. The trace of ink particles released upstream of the cylinder shows that the mainstream flow is skewed towards the upper endwall as it approaches the leading edge of the cylinder. Some of the injected ink particles follow the contour of the cylinder before they are separated from the cylinder surface. The wakes shed from the cylinder feed fluid with spanwise velocity into the aft cylinder, forming a jet-like flow. This fluid is then driven towards the upper endwall and impinges onto it. This jet-like flow is the main source of the high momentum flow region at the aft cylinder. Furthermore, since the jet-like flow behaves as crossflow to the wakes shed from the cylinder, it induces increased mixing of the mainstream flow behind the cylinder.

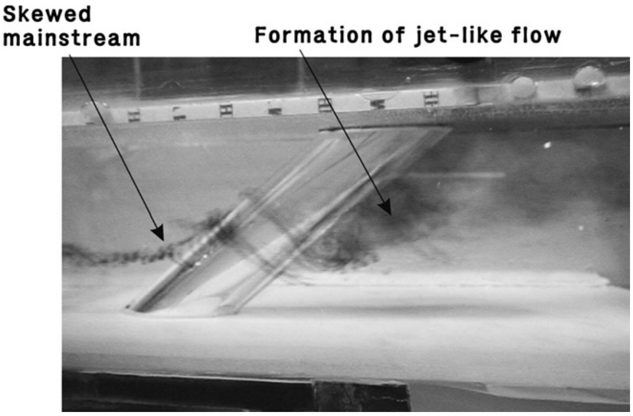

Fig. 7. Instantaneous image of streamlines around the 45° inclined cylinder obtained from the water-tunnel experiments at $Re_D = 1.0 \times 10^4$.

4.2. Flows on the cylinder surface

The time-averaged trace of the mainstream on the upright cylinder surface is shown in Fig. 8(a). After the mainstream flow stagnates onto the leading edge of the cylinder, it follows the contour of the cylinder until separation from the cylinder surface. The flow separation occurs at approximately 90° measured from the leading edge. The spanwise locations of the flow separation points configure a straight line parallel to the cylinder axis. The cylindrical surface regions near the both endwalls, especially at the leading and trailing edges of the cylinder, show footprints of secondary flows. With inclination, the separation line is no longer parallel to the cylinder axis (Fig. 8(b)). Close to the upper endwall, early separation takes place.

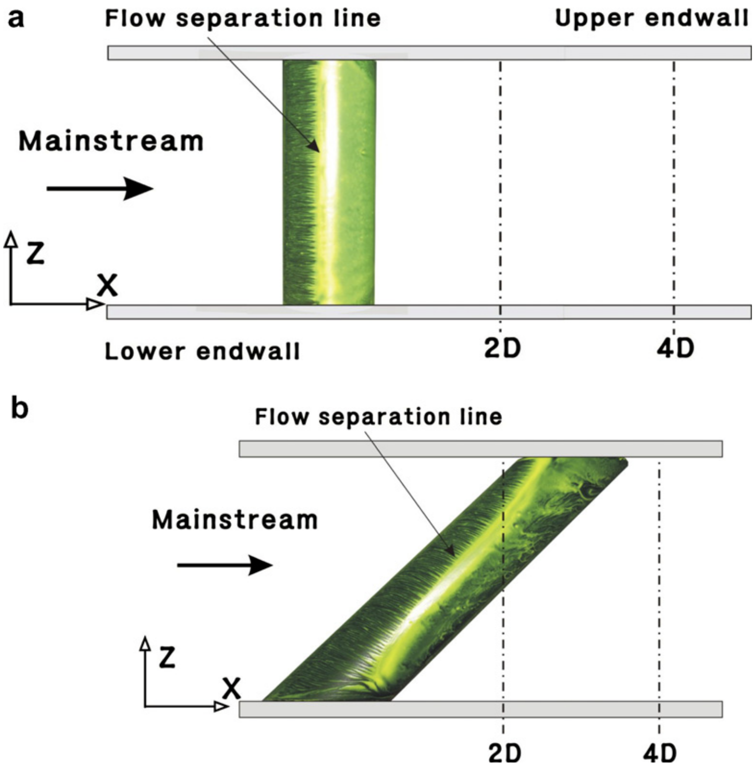

Fig. 8. Visualized cylinder surface flow patterns at $Re_D = 1.0 \times 10^4$: (a) 0°; (b) 45°.

Furthermore, before the separation, the streamlines of the flow on the cylinder surface are not perpendicular to the cylinder axis, implying that the "principle of independence" is invalid in the current short aspect ratio case.

4.3. Analysis

Based on the previous observations, the consequences of the inclination can be summarized as follows. Firstly, the mainstream gets skewed towards the upper endwall as it approaches the cylinder leading edge. Secondly, the flow separation line deviates from the cylinder axis. Thirdly, a jet-like flow forms immediately behind the cylinder and is driven towards the upper endwall. A sketch of the flow patterns is shown in Fig. 9. To analyze why the mainstream flow is skewed, two adjacent imaginary streamlines along the cylinder centerline, e.g., z and $z + \mathrm{d}z$, in $x = a$ (or a') and $x = b$ (or b') at $y = 0$ are considered. In this region, the static pressure acts towards the streamline of $z + \mathrm{d}z$, i.e., $\mathrm{d}p/\mathrm{d}z < 0$. The extent of the tendency increases as the flow convects downstream until $x = b$ (or b') due to the potential effect of the cylinder. While the flow follows the contour of the cylinder before its separation, the static pressure decreases. This results in a positive pressure gradient ($\mathrm{d}p/\mathrm{d}z > 0$) at $b < \times < c$. In addition, at each endwall, zero pressure gradient in the z'-axis is expected as negligible pressure gradient is present in the boundary layer of secondary flows along the direction normal to the endwall surface.

The three regions may be summarized as

(1) In $x = a$ (or a') and $x = b$ (or b'), before the stagnation: $\mathrm{d}p/\mathrm{d}z < 0$;
(2) In $x = b$ (or b') and $x = c$ (or c'), from the leading edge until the separation: $\mathrm{d}p/\mathrm{d}z > 0$;
(3) In $x = d$ and $x = d'$, near endwalls: $\mathrm{d}p/\mathrm{d}z = 0$;

where $\mathrm{d}p/\mathrm{d}z$ is the static pressure gradient along the channel height for a given axial location.

To examine the skewed separation line along the cylinder span from the cylinder axis, local pressure and velocity field across the streamlines are considered. The *local* stagnation pressure whose magnitude is proportional to the square of local shear velocity establishes a spanwise pressure gradient [19]. Due to the inclination, the mainstream velocity in the upper half of the channel is larger than that in the lower half for a given axial location (x-axis). In other words, lower velocity and hence lower stagnation pressure loss is expected to exist in the lower portion of the cylinder while higher velocity and higher loss exist in the upper portion before the mainstream passes the cylinder. The local shear velocity acts towards the lower part of the cylinder span, inducing a secondary flow velocity (W_p).

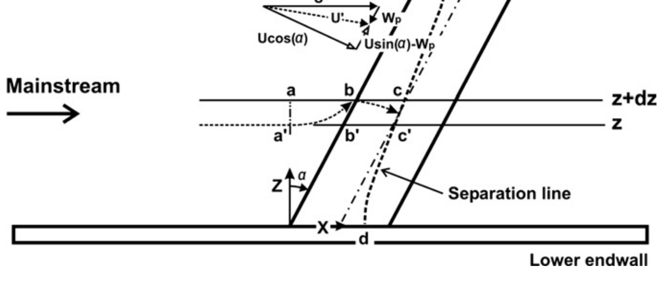

Fig. 9. Analytical sketch of the skewed mainstream flow and skewed flow separation line from the cylinder axis (z').

Decomposition of the mainstream velocity (U) yields $U\sin(\alpha)$ and $U\cos(\alpha)$, corresponding to the spanwise and normal components, respectively. The induced spanwise velocity (W_p), acting opposite to $U\sin(\alpha)$, reduces the magnitude of the *net* spanwise velocity of the mainstream flow, i.e. $U_{z'} = U\sin(\alpha) - W_\mathrm{p}$. Consequently, this leads to the non-perpendicular incidence to the cylinder axis. Moreover, the difference between the pressures before and after the separation line varies along span of the cylinder. Due to the jet-like flow, the flow is concentrated near the region on the upper endwall and the pressure in that region increases accordingly. Therefore, the separation position near the upper endwall is pushed towards the leading edge of the cylinder compared to that on the lower endwall, showing the skewed separation line along the cylinder span from the cylinder axis.

5. Downstream flow fields

5.1. Upright cylinder

At midspan in the x–y plane, the wake shedding patterns including the width of alternating wakes are sensitive to the inclination of the cylinder. The mainstream flow is also turned pitchwise, or skewed (in the z–x plane), by the inclined cylinder. This skewed mainstream flow is thought to interact with the lower/upper endwalls. To examine how the presence of the inclined cylinder affects the flow downstream of the cylinder, the flow angles and velocities were measured at two selected downstream traverse planes – $2D$ and $4D$ – from the cylinder axis on the lower endwall.

Fig. 10(a) presents spanwise variation of the area-averaged pitch angles for the upright cylinder case, covering transverse range near the cylinder i.e. $(-)1.5 \leqslant y/D \leqslant (+)1.5$ for each selected spanwise location, z-axis, where only the lower half of the cylinder span is considered. Near the lower endwall, the mainstream shows negative pitch angles. In this paper, a positive sign of the pitch angle denotes the flow directing downward to the lower endwall. Due to the boundary layers on the endwall surfaces (not quantified here), the flow is displaced from the endwall. Thus, streamlines near the lower endwall are directed towards the midspan, showing the

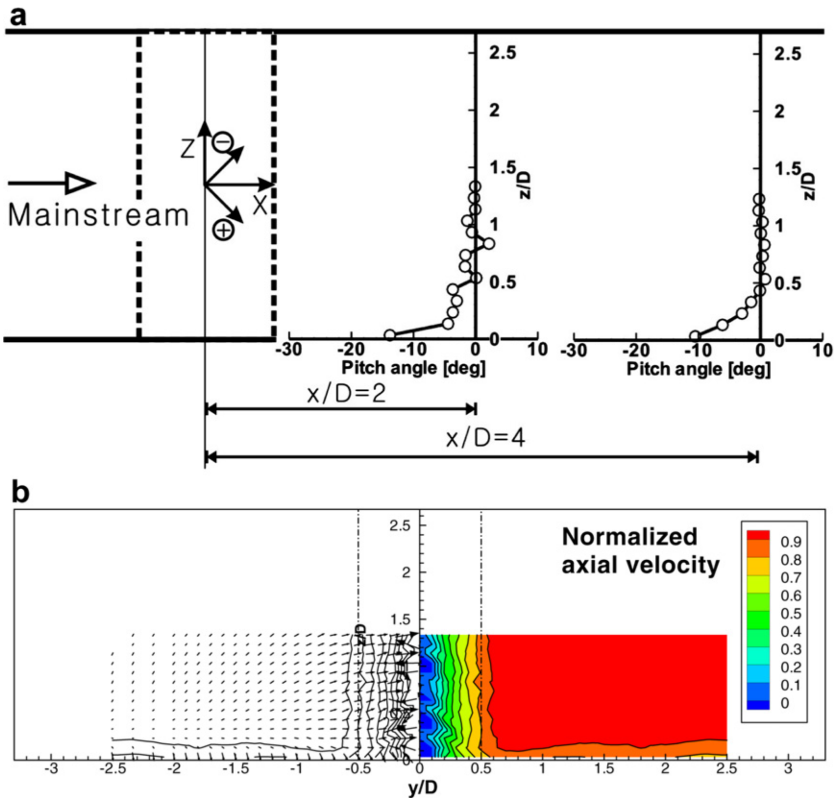

Fig. 10. Flow behind the upright cylinder at $Re_D = 1.0 \times 10^4$: (a) Flow turning by the cylinder; (b) Axial velocity contours (right half) and y–z plane velocity vectors (left half) behind the cylinder at $2D$.

negative pitch angles. Moving away from the lower endwall, the flow pitch angle decreases. The mainstream flow from $z/D \sim 0.5$ to $z/D \sim 1.35$ (midspan) has 0° pitch angle.

Fig. 10(b) shows separately the y–z velocity vectors (left side) and the contour of axial velocity normalized by the inlet mainstream velocity (right side) at the $x/D = 2.0$ plane. A large gradient of the axial velocity is concentrated near the cylinder edge ($y/D = \pm 0.5$) along the cylinder span where the flow separates. The y–z velocity vectors also indicate that the flow is directed towards the cylinder axis, i.e., $y/D = 0$ due to the vorticity filament formed parallel to the cylinder axis. In addition, there is a negative axial velocity region aligned with the cylinder axis displayed as zero velocity. With the five-hole probe, the negative velocity region could not be measured. This region implies a recirculating flow. Another velocity gradient observed near the endwall is due to the wall boundary layer. However, its gradient is not as large as that aligned with the cylinder span.

5.2. Inclined cylinders

The mainstream flow is skewed by the inclined cylinder. To quantify the flow turning, the pitch angles have been measured for a cylinder with 45° inclination, and the corresponding results are plotted in Fig. 11(a). The flow at $0 \leqslant z/D \leqslant 1.5$ is under the direct influence of the separated flow from the cylinder while that at $1.5 \leqslant z/D \leqslant 2.67$ is passing by the side of the cylinder, where $z/D = 0$ and 2.67 denote the locations of the lower and upper endwalls, respectively. For the same reason as in the upright cylinder case, the flow near the lower endwall shows negative pitch angles. Away from the lower endwall, the flow has a positive pitch angle, heading towards the lower endwall at $0.1 \leqslant z/D \leqslant 0.8$. When the mainstream flow separates from the cylinder surface, it is turned, resulting in a positive pitch angle. However, at $z/D = 0.8$, there exists a sudden change in the sign of the pitch angle, from positive to negative, due to the presence of the jet-like flow immediately downstream of the cylinder, at $0.8 \leqslant z/D \leqslant 1.1$. The velocity vectors shown in Fig. 11(b) clearly indicate the formation of two counter-rotating vortices. The mainstream, then, flows parallel to the endwalls before its angle gradually becomes positive, which is associated with the separated flow from the leading edge of the upper endwall vertex.

At $x/D = 4$ (Fig. 11(c)), the flow in the lower half near the lower endwall flows in general downward (positive pitch angle) while that in the upper half shows flows towards the upper endwall. A very large gradient of the pitch angle is clearly seen at $1.5 \leqslant z/D \leqslant 2.2$. This region is associated with the approach of the jet-like flow to the upper endwall. Clearly, two counter-rotating vortices are

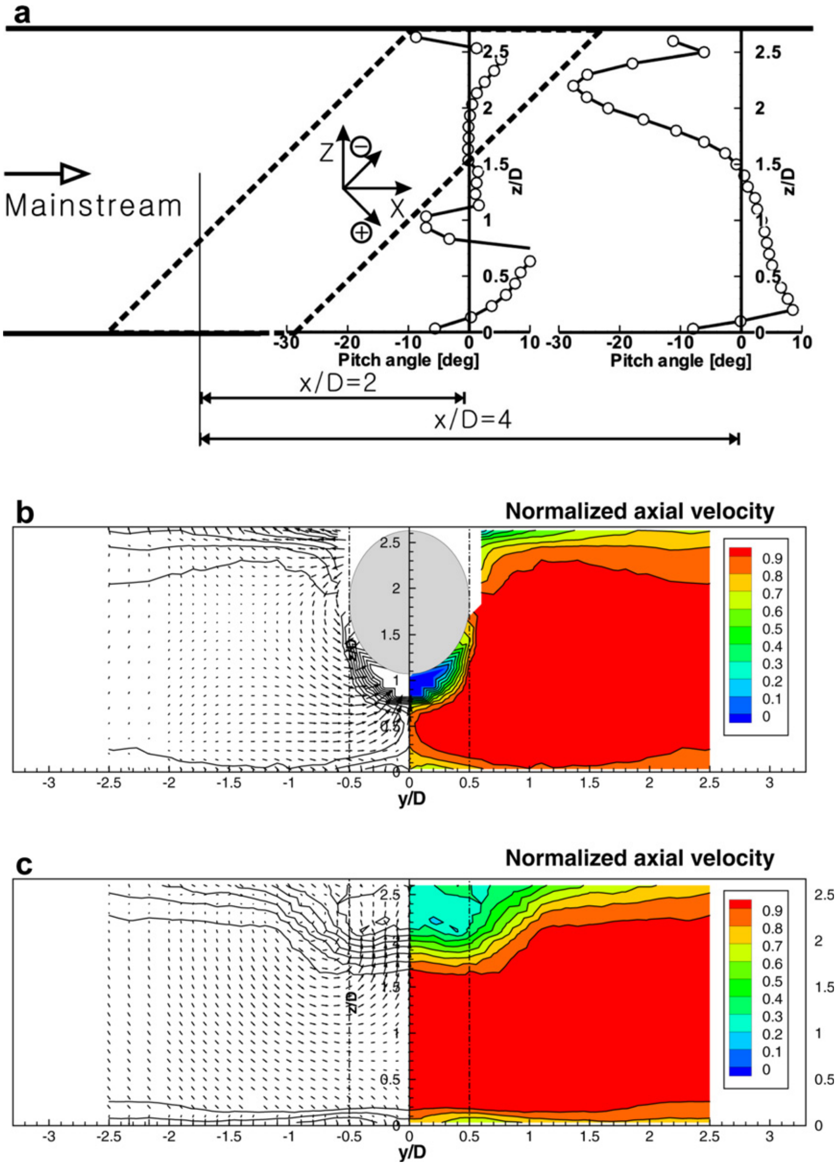

Fig. 11. Flow behind the 45° inclined cylinder at $Re_D = 1.0 \times 10^4$: (a) flow turning by the cylinder; (b) axial velocity contours (right half) and y–z plane velocity vectors (left half) behind the cylinder at $2D$; and (c) at $4D$.

visible. The pitch angles increase, resulting from the interaction with horseshoe vortex formed around the upper endwall. The low axial momentum vortical core of the horseshoe vortex acts to reduce the pitch angle of the flow near the upper endwall. The jet-like flow accumulates behind the upper part of the cylinder and convects downstream. The axial velocity behind the lower cylinder part has fully recovered to the mainstream value.

6. Sketch of flows around inclined single cylinder

The flows induced by the inclination affecting the endwall heat transfer on the both endwalls can be summarized as follows. Fig. 12 also illustrates the flows around the inclined cylinder. First, the inlet boundary layers develop as the mainstream flow convects downstream. When the mainstream approaches the leading edge of the cylinder, the inlet boundary layer vorticity is obstructed by the cylinder. Since the boundary layer vorticity cannot be destroyed, it is, instead, convected around each side of the cylinder to form the two legs of the horseshoe vortex. Second, on the lower endwall, they interact with wakes shed from the inclined cylinder, obstructing their tails. In the footprint of their interaction marked on the lower endwall, the parabolic curve reflects the projection of the mean wake width. Third, a jet-like flow due to the two counter-rotating vortices impinges onto the upper endwall. Due to the jet-like flow, the momentum of the flow at this region is increased. Thus, the mixing between the impinged flow and horseshoe vortex is enhanced, leading to a wide region

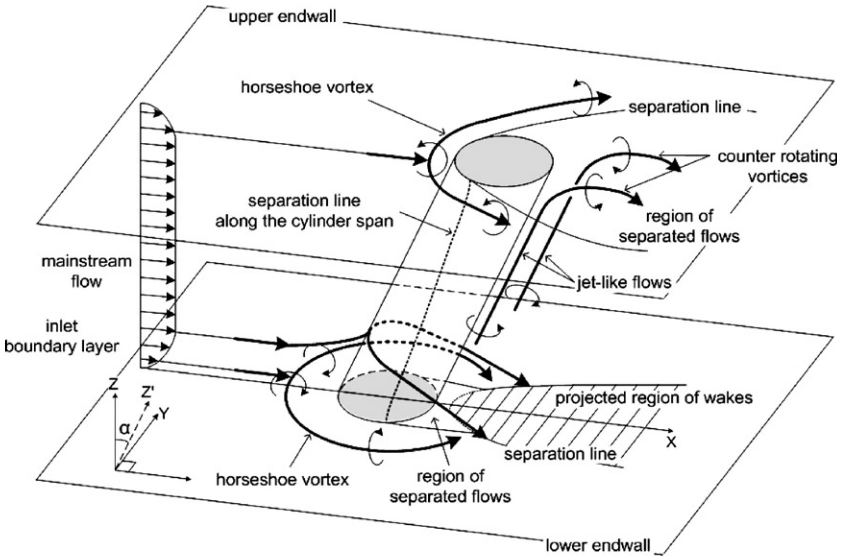

Fig. 12. Schematic of the time-averaged flow features around a cylinder confined between endwalls with a finite inclined angle.

of enhanced heat transfer aft of the cylinder on the endwall.

7. Conclusions

A series of experiments to examine the effects of cylinder inclination on the flows and heat transfer at the endwall and on the surfaces of a single cylinder has been performed. The local and overall behaviors of the endwall heat transfer strongly depend on the direction and magnitude of the cylinder inclination relative to the endwall. Due to the short aspect ratio of the cylinder whose both ends are attached to the endwalls, the principle of independence does not hold. The flow features on the cylinder/endwall surfaces induced by the inclination can be summarized as follows:

(1) As a result of the inclination of the cylinder, the mainstream approaching the foreside of the cylinder is skewed due to the pressure gradient along the span.
(2) The separation line is misaligned with the cylinder axis because the inclination of the cylinder generates an additional velocity component which acts to reduce the velocity component of the mainstream flow parallel to the cylinder axis.
(3) A jet-like flow is generated downstream of the cylinder, which then impinges onto the upper endwall surface.
(4) For cylinder inclination angles smaller than 45°, the heat transfer on the lower endwall is enhanced due to the impingement of the wakes shed from the cylinder.
(5) For cylinder inclination less than 45°, the heat transfer on the upper endwall is enhanced due to the impingement of the jet-like flow and is broadened as a result of the interaction between the horseshoe vortex and the jet-like flow.

Acknowledgements

This work was financially supported by the Microthermal System Research Center of KOSEF/MOST (Grant number R11-2001-095-02002-0); BK21 of MOE of Korea; the National Basic Research Program of China (Grant number 2006CB601202); and the National Natural Science Foundation of China (Grant numbers 10328203 and 10572111).

References

[1] M. Jacob, Heat Transfer, vol. 1, Wiley, New York, 1949.
[2] A. Zukauskas, Heat transfer from tubes in crossflow, Adv. Heat Transfer 18 (1987) 87–159.
[3] M.M. Zdravkovich, Flow Around Circular Cylinders. Vol. 1: Fundamentals, Oxford Science Publications, 1997.
[4] M.M. Zdravkovich, Flow Around Circular Cylinders. Vol. 2, Oxford Science Publications, 2003.
[5] W.M. Yan, R.C. Hsieh, C.Y. Soong, Experimental study of surface-mounted obstacle effects on heat transfer enhancement by using transient liquid crystal thermograph, J. Heat Transfer 124 (2002) 762–769.
[6] E.M. Sparrow, A.A. Yanez Moreno, Effect of yaw on forced convection heat transfer from a circular cylinder, Int. J. Heat Mass Transfer 30 (1987) 427–436.
[7] V. Mansingh, P.H. Oosthuizen, Free and forced convection heat transfer from short inclined circular cylinders, Chem. Eng. Commun. 42 (1986) 333–348.
[8] D. Sumner, J.L. Heseltine, O.J.P. Dansereau, Wake structure of a finite circular cylinder of small aspect ratio, Exp. Fluids 37 (2004) 720–730.
[9] P.T. Ireland, A.J. Neely, D.R.H. Gillespie, A.J. Robertson, Turbulent heat transfer measurements using liquid crystal, Int. J. Heat Fluid Flow 20 (1999) 355–367.
[10] Y. Yan, J.M. Owen, Uncertainties in transient heat transfer measurements with liquid crystal, Int. J. Heat Mass Transfer 23 (2002) 29–35.
[11] P.J. Newton, Y. Yan, N.E. Stevens, S.T. Evatt, G.D. Lock, J.M. Owen, Transient heat transfer measurements using thermochromic

liquid crystal. Part 1: An improved technique, Int. J. Heat Fluid Flow 24 (2003) 14–22.

[12] D.R.H. Gillespie, Intricate internal cooling systems for gas turbine blading, D. Phil. Thesis, Department of Engineering Science, University of Oxford, UK, 1996.

[13] H.W. Coleman, W.G. Steele, Experimentation and uncertainty analysis for engineers, 2nd ed., John Wiley and Sons, New York, 1999.

[14] T. Kim, Fluid-flow and heat transfer in a lattice-frame material, Ph.D. Thesis, Department of Engineering, University of Cambridge, UK, 2004.

[15] F.P. Incropera, D.P. DeWitt, Fundamentals of Heat and Mass Transfer, 3rd ed., Wiley, NY, 1990.

[16] T.J. Praisner, D.R. Sabatino, C.R. Smith, Simultaneously combined liquid crystal surface heat transfer and PIV flow-field measurements, Exp. Fluids 30 (2001) 1–10.

[17] J.C.R. Hunt, C.J. Abell, J.A. Petetka, H. Woo, Kinematical studies of the flows around free or surface-mounted obstacles; applying topology to flow visualization, J. Fluid Mech. 86 (1978) 79–200.

[18] I.K. Choi, The variation of wakes and horseshoe vortices due to the inclination of a short single cylinder, B. Eng. Thesis, School of Mechanical and Aerospace Engineering, Seoul National University, Korea, 2005.

[19] E.M. Greitzer, C.S. Tan, M.B. Graf, Internal Flow: Concept and Applications, Cambridge University Press, 2004.